www.advenergymat.de

Regulation of 3*d*-Transition Metal Interlayered Disorder by Appropriate Lithium Depletion for Li-Rich Layered Oxide with Remarkably Enhanced Initial Coulombic Efficiency and Stability

Ying Zhang, Zhefeng Chen, Xiaoyu Shi, Caixia Meng, Pratteek Das, Shuanghao Zheng, Feng Pan,* and Zhong-Shuai Wu*

Li-rich materials are among the most promising cathode materials for lithiumion batteries thanks to their high specific capacity. However, they exhibit poor structural stability, resulting in low initial Coulombic efficiency and limited cycle stability. Herein, a long-neglected Li-deficient state is realized for a Co-free lithium-rich cathode through a facile calcination medium-induced surface-corrosion (CMISC) strategy for alleviating the aforementioned drawbacks. The as-constructed Li-deficient lithium-rich cathode of Li_{1.2-\(\sigma\)}Mn_{0.6}Ni_{0.2}O₂ (d-LMNO) exhibits an enhanced capacity of 272 mAh g⁻¹, improved initial efficiency of 84.5%, and cycle stability with 82.0% retention over 200 cycles. In addition, multiple in situ and ex situ investigations confirm the appropriate lithium depletion regulated 3d-transition metal interlayered disorder, resulting in excellent structural reversibility of d-LMNO. Also, theory simulations suggest that the crystal structure with Li-defects has lower energy and Li-diffusion energy barrier when the coordination interlayer 3d-metal has more Ni closer to the diffused Li, meaning less interlayered disorder. And the migration of Li close to the vacancy is dominated by a tetrahedral site hopping path in the presence of additional vacancies around the Li vacancy, which has a low migration energy barrier. Moreover, similar results achieved in Co-containing Li-rich cathodes further demonstrate the universality of this simple CMISC strategy, exhibiting great potential for performance improvement and applicability.

1. Introduction

Developing high-performance lithium battery technology is crucial for the advancements in various applications ranging from consumer electronics to electric vehicles.^[1,2] To attain

this objective, cathode materials must be improved further to achieve a longer operation lifetime, lower production cost, better safety, and environmental friendliness. Attributed to low cost, resource abundance, and high specific capacity (>250 mAh g⁻¹), cobalt-free Li-rich layered 3d-transition-metal (TM) oxides have attracted widespread attention as a class of promising cathode materials to compete with the current commercial counterparts. [3,4] In terms of crystal structure, Li-rich oxides can be thought of an ordered rock-salt derivative (LiTMO₂, $R\overline{3}m$), in which octahedrally coordinated TM and Li cations preferably form alternating layers linked by the interlayer oxygen, and supplemented by a superlattice (Li₂MnO₃, C2/m, also written as 3/2 (Li(Li_{1/3}Mn_{2/3}) O₂)) formed by substituting 1/3 TM cations with Li in TM layer (Figure 1a).[5] The unique structure allows the anionic $(O^{2-} \rightarrow (O_2)^{n-}, 1 \le n < 3)$ redox processes in Li-rich cathodes, which are responsible for the excessive capacity contribution compared to normal layered oxides.^[5-7] Nonetheless, the anionic redox reaction

inevitably leads to O–O dimerization and oxygen release to some degree, $^{[8,9]}$ which expedites the activation of lower-voltage $\rm Mn^{3+}/Mn^{4+}$ redox couple during cycling. $^{[10]}$ Meanwhile, the migration of partial TM cations into the Li layers leads to the generation of the $TM_{\rm Li}$ - $V_{\rm TM}$ antisite cation-vacancy defects, $^{[11-17]}$

Y. Zhang, X. Shi, C. Meng, P. Das, S. Zheng, Z.-S. Wu State Key Laboratory of Catalysis Dalian Institute of Chemical Physics Chinese Academy of Sciences 457 Zhongshan Road, Dalian 116023, China E-mail: wuzs@dicp.ac.cn Y. Zhang, P. Das University of Chinese Academy of Sciences 19 A Yuquan Road, Beijing 100049, China

The ORCID identification number(s) for the author(s) of this article can be found under https://doi.org/10.1002/aenm.202203045.

Z. Chen, F. Pan
School of Advanced Materials
Peking University
Shenzhen Graduate School
Shenzhen 518055, China
E-mail: panfeng@pkusz.edu.cn
S. Zheng, Z.-S. Wu
Dalian National Laboratory for Clean Energy
Chinese Academy of Sciences
457 Zhongshan Road, Dalian 116023, China

DOI: 10.1002/aenm.202203045

16146840, 2023, 5, Downloaded from https://advanced.

onlinelblary.wiley.com/doi/10.1002/anm.202203045 by University Town Of Shenzhen. Wiley Online Library on [2011/2025]. See the Terms and Conditions (thps://onlinelblary.wiley.com/terms-and-conditions) on Wiley Online Library for rules of use; OA articles are governed by the applicable Creative Commons.

www.advancedsciencenews.com www.advenergymat.de

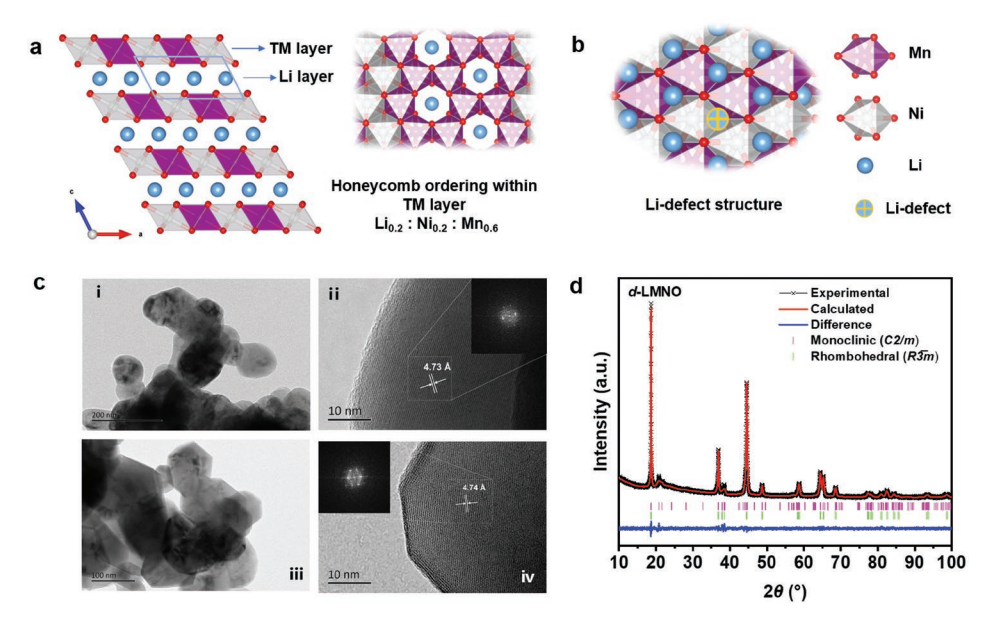


Figure 1. Crystal structures and characterizations of d-LMNO and n-LMNO. a) A possible configuration for n-LMNO with a layered $R\overline{3}m$ and monoclinic C2/m symmetry, and a honeycomb ordering within the TM cation layer. b) Crystal structure of Li layer for d-LMNO. c) HRTEM images and FFT (inset) of the selected area of i,ii) n-LMNO and iii,iv) d-LMNO. d) Rietveld refinement of XRD patterns for d-LMNO.

which is a direct factor of the voltage fading.^[7,18] Additionally, this interlayer TM disorder eventually causes Li site energies to be perturbed during the lithiation/delithiation process^[15,19–21] and lowers the redox potential of Li-rich cathodes,^[22] resulting in low initial efficiency, serious voltage hysteresis, sluggish kinetics, and irreversible structural phase change, which are the main issues plaguing the present generation of Li-rich cathode materials.^[4,6,12,16,23]

So far, several methodologies have already been reported to inhibit lattice oxygen escape and cation migration. For example, great efforts have been devoted to experimental and theoretical investigations into heteroatom-doped Li-rich cathodes, and some appropriate TM cation dopants (3d [Mn], 4d [Ru, Nb], 5d [Ir, Os, and Ta] metal elements) have been systematically explored and screened, such as Li₂Ru_{1-v}Sn_vO₃, β-Li₂IrO₃, and Ta-doped Li_{1.3}Nb_{0.3}Mn_{0.4}O₂. [5,11,24-27] Further, anion-cation co-doping, combining high-valence cations and partial replacement of oxygen with fluorine, was applied for introducing reversible Mn²⁺/Mn⁴⁺ redox couple to avoid excessive activation of oxygen and maintain structural integrity.[1] Strategies like surface coatings and surface polyanion modification have also been evidenced as effective methods.[10,28] Furthermore, some other solutions including tuning local symmetry,[8] forming Li₂ZrO₃ slabs into Li₂MnO₃ domains tensioning the metaloxygen link, [29] and introducing non-topotactic reactions have also been proposed to fundamentally inhibit lattice oxygen escape and cation migration.[30] Recently, it is reported that the driving force for voltage fade is the lattice displacement/ strain that is induced by heterogeneous composite structures (LiTMO2 and Li2MnO3).[31] So far, most of the methods listed above focus on the lattice oxygen escape aiming to relieve voltage fading, improve rate capability, and enhance cycle stability. However, the irreversible lattice oxygen release is also to blame for the low initial Coulombic efficiency. Hence, simple methods and novel concepts are still required to improve the Coulombic efficiency in the first cycle, which closely correlates to the subsequent structural stability, but has been overlooked for a long time.

Recent research suggests that the primary determinant to activate the lattice oxygen is not the TM migration itself, but the resulting trapping of TM ions in the Li layers, [23] and the TM-deficient environment near oxygen also plays a critical role in activating the lattice oxygen in Li-rich layered materials.^[32–35] Moreover, researchers recently proposed a Li-gradient construction method to eliminate O₂ release.^[3] Typically, it is noted that the O2 from the O-redox likely gets trapped in the bulk and some are lost from the surface.^[21] These findings are critical and inspire us to modify the TM-deficient environment and further stabilize lattice oxygen by constructing a Li-deficient environment around the O on the surface of Li-rich layered materials. However, few simple strategies have been proposed to approach the problem from the perspective of surface Lidefects. Furthermore, introducing the Li-defects into low-cost cobalt-free Li-rich cathodes, to some extent, would assist in the prevention of excessive oxygen release and structure collapse during the activation in the first cycle, thereby improving initial efficiency and subsequent cyclic stability.

To address this, we present a general and simple strategy for creating surface lithium defects in cobalt-free Li-rich cathodes with greatly enhanced initial efficiency and stability through the calcination medium-induced surface-corrosion (CMISC) method. The achieved Li-rich material Li_{1.2-o}Mn_{0.6}Ni_{0.2}O₂ in the appropriate Li-defect state (denoted as *d*-LMNO) achieved an improved initial efficiency of 84.5%, and an enhanced discharge capacity of 272 mAh g⁻¹ in the first cycle compared to the pristine materials (64.1%, 243 mAh g⁻¹), and it could even give out more than 82.0% capacity retention after 200 cycles, much exceeding the counterparts with normal Li content (Li_{1.2}Ni_{0.2}Mn_{0.6}O₂, denoted as *n*-LMNO). Furthermore, multiple in situ and ex situ characterizations combined with synchrotron

www.advenergymat.de

16146840, 2023, 5, Downloaded from https://advancedonlinelibrary.wiley.com/doi/10.1002/aenm.202203045 by University Town Of Shenzhen, Wiley Online Library on [2011/2025]. See the Terms and Conditions (https://onlinelibrary.wiley.com/erms-and-conditions) on Wiley Online Library for rules of use; OA articles are governed by the applicable Creative Commons Licensen

X-ray absorption spectroscopy (XAS) were performed to further reveal structural evolution and information on the local atomic structure during the first charge and discharge process. These techniques comprehensively verify the appropriate lithium depletion regulated 3d-transition metal interlayered disorder, resulting in excellent reversibility and structural stability of d-LMNO. In addition, the density functional theoretical (DFT) simulation indicates that the crystal structure with Li-defects has lower energy and Li-diffusion energy barrier when the coordination interlayer 3d-metal has more Ni closest to the diffused Li, meaning less interlayered disorder. And the migration of the Li close to the vacancy is dominated by a tetrahedral site hopping path in the presence of additional vacancies around the Li vacancy, which has a low migration energy barrier. Finally, the simple construction strategy of the Li-defects was also applied in cobalt-containing Li-rich materials (d-LMNCO) to obtain enhanced performance and consistent structural transformation, which further confirmed the universality and great potential of the CMISC method in constructing high-performance Li-rich cathodes.

2. Results and Discussion

2.1. Structural Characterization of d-LMNO

The crystal structures of the as-prepared Li-rich materials possess a layered $R\overline{3}m$ and monoclinic C2/m symmetry, and the schematic diagrams of d-LMNO with appropriate Li-defects were shown in Figure 1a,b. To elucidate the morphology and crystal structure of d-LMNO and n-LMNO, high-resolution transmission electron microscopy (HRTEM) was examined. It is revealed that the primary particle morphology of n-LMNO is closer to spheroid, while the d-LMNO particles are primarily polyhedron-shaped with better crystallinity (Figure 1c). Fast Fourier transform (FFT) of the selected area and lattice stripes with a crystal plane spacing of 4.73 or 4.74 Å can be observed in Figure 1c. It is indicated that layered structures are successfully formed in both n-LMNO and d-LMNO.

Further, by using inductively coupled plasma optical emission spectrometry (ICP-OES) measurement to quantify the lithium defects, it is calculated that the lithium content in d-LMNO is equivalent to 94% of that in *n*-LMNO (Table S1, Supporting Information), indicating a lithium depletion of 6%. Thus, it is validated that the d-LMNO obtained through the CMISC method is in a Li-defect state (Figure 1b). Secondly, a significant change from X-ray diffraction (XRD) patterns is observed in the quartz boat, while that from the ceramic boat does not show any change after calcination (Figure S1, Supporting Information). It is speculated that the Li-defects are caused by corrosion resistance difference towards as-prepared Li-rich cathodes between ceramic boat and quartz boat during the calcination, in which the Li at the surface of n-LMNO is possibly consumed by corroding quartz calcination medium to form Li-containing oxides. [36,37] Furthermore, no Si elements are detected for both n-LMNO and d-LMNO (Figure S2, Supporting Information), manifesting that this CMISC technique can avoid the introduction of Si-containing oxides, particularly from SiO2-based quartz calcination medium for d-LMNO. In short, it is proved that the CMISC strategy is effective to create Li defects without destroying the samples. Also, it is confirmed from electron paramagnetic resonance (EPR) that *d*-LMNO possesses a higher signal, which may arise from the presence of more magnetic clusters near Li defects in *d*-LMNO with a smaller lithium-ion binding, thereby leading to a stronger magnetic interaction (Figure S3, Supporting Information).

To explore if the lithium depletion during calcination results in the structural change of Li-rich cathode materials, XRD patterns are refined through the conventional Rietveld method. Notably, both n-LMNO and d-LMNO exhibit similar peaks, which are indexed to C2/m and $R\overline{3}m$ phases (Figure 1d, and Figure S4, Supporting Information). Nevertheless, the C2/m phase of d-LMNO possesses larger structure parameters and slightly expands cell volume of 201.148 Å 3 compared to n-LMNO (200.393 Å 3), which is expected to be beneficial for Li-ion diffusion during the charge and discharge process. [38] In comparison, no obvious difference is observed in the $R\overline{3}m$ phase (Table S2, Supporting Information).

2.2. Electrochemical Performance of d-LMNO

To confirm the effect of lithium depletion on the performance of the Li-rich cathode, the electrochemical properties of n-LMNO and d-LMNO were systemically evaluated. From Figure 2a, it is observed that d-LMNO delivers a specific capacity of 272 mAh g⁻¹ and an initial Coulombic efficiency of 84.5% under the current density of 0.1 C (25 mA g⁻¹) within 2.0–4.8 V, much higher than that of n-LMNO (243 mAh g⁻¹, 64.1%). As mentioned earlier, the low initial efficiency of n-LMNO is attributed to the anionic oxidation accompanied by irreversible oxygen release and TM migration to Li+ sites. In contrast, d-LMNO displays a lower charge capacity contribution from anion oxidation which is clear from the weaker oxidation peak of d-LMNO at ≈4.5 V than n-LMNO (Figure 2b). Cyclic voltammetry (CV) curves certainly illustrate the activation process. As shown in Figure S5, Supporting Information, the CV curves of *n*-LMNO shows a weak peak at \approx 3.94 V and a strong peak at ≈4.7 V in the initial positive scan, corresponding to the oxidation of $Ni^{2+} \rightarrow Ni^{3+}/Ni^{4+}$ and $O^{2-} \rightarrow O^{n-}$, respectively. It is consistent with the charge-discharge profiles with the lower capacity contribution from Ni²⁺→Ni³⁺/Ni⁴⁺ (Figure 2a) and the initial dQ/dV curves with more oxygen release (Figure 2b). In the negative scan, the broad peak above 3.78 V corresponds to the reduction of Ni⁴⁺. Besides, the partial reduction of Mn⁴⁺ is accompanied by the conversion from $(O_2)^{n-}$ to O^{2-} (1 < n < 3) at ≈3.26 V due to the voltage hysteresis from anionic redox reactions.^[15] By comparison, the d-LMNO exhibits a weaker oxidation peak at ≈4.7 V in the first charge process and more Ni⁴⁺ reduction to Ni²⁺ above 3.78 V during discharging, representing less O2 release and superior reversibility due to the Li-defect structure of *d*-LMNO.

The effects of Li-depletion can also be seen in the kinetics of d-LMNO and n-LMNO. The galvanostatic intermittent titration technique (GITT) was employed to estimate the Li⁺ diffusion coefficient ($D_{\rm Li}^+$) in the charge-discharge process (Figure S6, Supporting Information). As shown in Figure 2c, $D_{\rm Li}^+$ exhibits higher values before charging to 4.5 V, corresponding to fast

www.advenergymat.de

16146840, 2023, 5, Downloaded from https://adv

nlinelibrary.wiley.com/doi/10.1002/aenm.202203045 by University Town Of Shenzhen, Wiley Online Library on [20/11/2025]. See the Terms and Conditions (https://onlinelibrary.wiley.com/terms

and-conditions) on Wiley Online Library for rules of use; OA articles are governed by the applicable Creative Commons

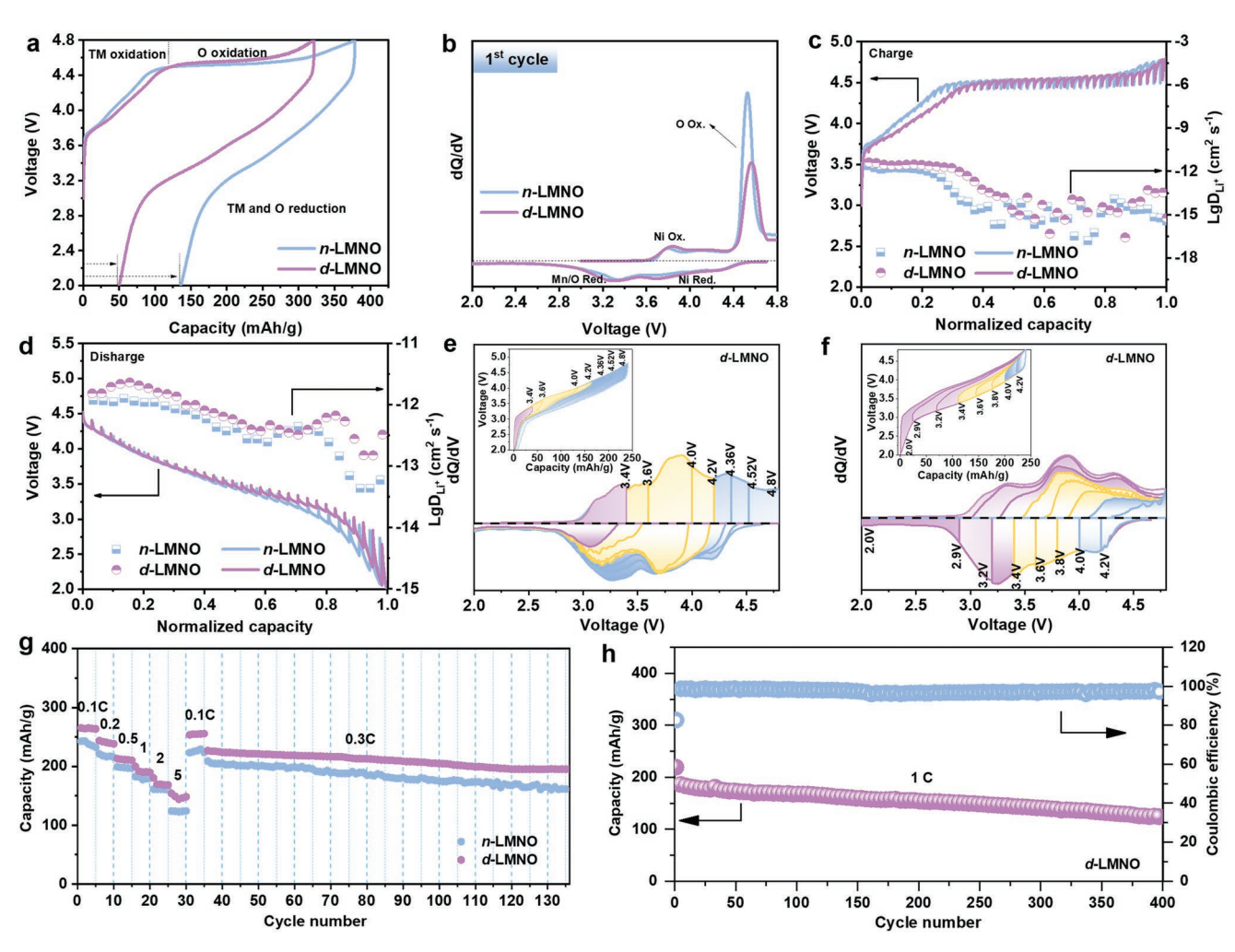


Figure 2. Electrochemical performance and kinetic behavior of d-LMNO and n-LMNO. a) The charge-discharge curve in the first cycle of d-LMNO and n-LMNO at 0.1 C, and b) their corresponding differential capacity (dQ/dV) plot. c,d) GITT measurements in the first cycle and the corresponding D_{Li}^+ for c) charge and d) discharge process. e) Voltage profiles (inset) and corresponding dQ/dV curves of d-LMNO tested from 3.4 V to gradually increased charging window until 4.8 V. f) Voltage profiles (inset) and corresponding dQ/dV curves of d-LMNO tested from 4.8 V to gradually declined to discharge window until 2.0 V. Redox reactions from different elements in d-LMNO are distinguished with different colors in (e) and (f). g) The rate capability of d-LMNO and n-LMNO. h) The cycling performance of d-LMNO was obtained at 1 C.

kinetics of the cationic Ni²⁺/Ni⁴⁺ redox reactions. Relatively, lower D_{Li}^+ observed at high voltage (> 4.5 V) reflects the sluggish kinetics of anionic O²⁻/(O₂)ⁿ⁻ redox process compared to cationic Ni2+/Ni4+ redox in the charging process for both d-LMNO and *n*-LMNO.^[39] Meanwhile, the D_{Li}^+ of *d*-LMNO during charging is slightly higher than that of n-LMNO, suggestive of the positive effect of lithium defects on Li ion diffusion. During the discharge process, the D_{Li}^+ of d-LMNO is also higher than that of n-LMNO at the voltage above 3.4 V. While further discharging to 3.3 V, a different phenomenon is observed, in which the D_{Li}^+ of *n*-LMNO progressively declines and the one of d-LMNO rapidly increases, implying more obvious (O₂)ⁿ⁻/ O^{2-} lagging reduction in the *n*-LMNO (Figure 2d). It is validated that lithium defects in d-LMNO may mitigate the impact of $(O_2)^{n-}/O^{2-}$ reduction compared to n-LMNO. To characterize the electrochemical behavior after pre-activation, the n-LMNO and d-LMNO electrodes cycled ten times are further tested by performing every cycle from 2.0 V to a series of different cutoff voltages (from 3.4 to 4.8 V). Specifically, according to redox reactions from different elements, the corresponding dQ/dV curves are divided into three voltage ranges: i) low potential region (2.0-3.4 V), corresponding to capacity contribution mainly from the redox reaction of Mn³⁺/Mn⁴⁺; ii) medium potential region (3.4-4.2 V), corresponding to the contribution mainly from the redox reaction of Ni²⁺/Ni⁴⁺; and iii) high potential region (4.2-4.8 V), corresponding to capacity contribution mainly from the redox reaction of $O^{2-}/(O_2)^{n-}$. [39,40] Especially, it is notable that the charging capacity above 4.2 V could just be recovered partially during discharging, which was caused by the lagging O²⁻/(O₂)ⁿ⁻ reduction reaction, while the remaining oxygen is reduced below ≈3.3 V for *n*-LMNO (Figure S7a, Supporting Information) and $\approx 3.4 \text{ V}$ for d-LMNO (Figure 2e), as well as the more remaining oxygen reduced for n-LMNO, suggesting a more serious voltage hysteresis for n-LMNO. Further, the pre-activated n-LMNO and d-LMNO electrodes were also measured in the case that the discharge voltage window decreased

www.advenergymat.de

16146849, 2023, 5, Downloaded from https://dvancedonlinelibrary.wiley.com/doi/10.1002/aenna.020203045 by University Town Of Shenzhen, Wiley Online Library on [2011/1025]. See the Terms and Conditions (https://onlinelibrary.wiley.com/terms-and-conditions) on Wiley Online Library or rules of use; OA articles are governed by the applicable Creative Commons Licensen

successively to 2.0 V (starting from 4.8 V per scan). As shown in Figure 2f and Figure S7b, Supporting Information, when the discharge voltage is lower than 3.4 V, there still exists a part of oxygen being oxidized during charging, consistent with the hysteresis phenomenon in Figure 2e. Apparently, compared with *d*-LMNO, *n*-LMNO displays a sluggish Mn oxidation peak below 3.4 V, indicating that it possibly suffers from a reduction of Mn⁴⁺ to Mn³⁺ during the activation process. Thus more Mn⁴⁺/Mn³⁺ redox species contribute to the capacity in the charging process for subsequent cycles for *n*-LMNO, caused by more TM migration and oxygen release due to severe lattice strain for crystal structures and different electrochemical activities of LiTMO₂ and Li₂MnO₃.^[31]

Moreover, Li-depletion plays a positive role in boosting the rate capability and cycle stability of *d*-LMNO (Figure 2g), outputting a specific capacity as high as 150 mAh g⁻¹ at 5 C and more favorable retention than *n*-LMNO after 130 cycles at 0.3 C (Figure 2g). When the current density further increases to 1 C, *d*-LMNO could still maintain more than 82.0% initial capacity after 200 cycles (Figure 2h), exceeding 67.2% of *n*-LMNO after 200 cycles (Figure S8, Supporting Information). Further, the superior cycling performance is also demonstrated in the full cell based on graphite as the anode, presenting a high capacity retention of 83.4% after 200 cycles at 2 C (Figure S9, Supporting Information).

2.3. The First Cycle Reversibility Analysis of Structural Change for d-LMNO

To elucidate the structural stability difference of d-LMNO and n-LMNO, the in situ XRD measurements were performed to investigate the first cycle between 2.0-4.8 V. And the contour plots of the diffraction intensity for the peaks from (003), (101), (012), (104), and (107) crystal planes are represented by the color depth. From Figure 3a, it is notable that nearly all peaks in n-LMNO witness a great shift after discharging to 2.0 V, suggesting that the structure may have been rearranged. By contrast, in d-LMNO these peaks are well restored to the initial position after the first charge-discharge cycle (Figure 3b), indicating better structural reversibility. As reported previously, a higher initial efficiency during cycling points to benign changes in lattice parameters of excellent electrode materials. Further, the conducted ex situ XRD pattern analysis can more comprehensively reveal the long-range structural evolution of d-LMNO and *n*-LMNO during the first charge-discharge process. As expected, the adjacent peaks of (018)/(110) show a clear split, suggesting a typical layered structure of Li-rich materials.^[41,42] In addition, the (018) peak of these two cathodes gradually disappears when charging to 4.8 V. And it appears again when discharging to 4.0 V for d-LMNO, yet which is observed until 3.6 V for n-LMNO, further indicating better reversibility of d-LMNO (Figure S10, Supporting Information). This is also consistent with the in situ XRD measurements. Similar results are also obtained by ex situ Raman spectra of n-LMNO and d-LMNO. From Figure 3c,d, it is deduced that the A_{1g} peak of n-LMNO and d-LMNO shifts to a higher wavenumber in the process of charging to 4.8 V. However, the A_{1g} peak could be well restored to the initial position after discharging to 2.0 V

only in the *d*-LMNO, suggestive of superior structural reversibility of *d*-LMNO. Moreover, well-recovered Raman intensity contour images of *d*-LMNO also prove the preferred structural reversibility compared to *n*-LMNO (Figure 3e,f). Based on the observation of structure evolution during the initial cycle, such superior structural reversibility of *d*-LMNO effectively avoids structural degradation, resulting in favorable long-term cycling stability.

2.4. Local Atomic Structure Analysis

According to the redox reactions from cation and anion, the charge-discharge profile in the first cycle (Figure 4a) is divided into three regions: i) the sloping region <4.5 V in the charging process is vest in the oxidation of Ni species; ii) the plateau region above 4.5 V in charge process is assigned to the oxidation of O²⁻; and (iii) the discharge profile corresponds to the reduction of TM and O species. [21,43] To further probe the structural stability of the modified d-LMNO, more ex situ characterizations were carried out on the cathode materials at the different voltages marked in Figure 4a. First, ex situ Ni K-edge XAS spectra demonstrate the electrical stability of the softened structure caused by Li defects, responsible for improved reversibility. In general, the "white line" absorption features in the region near 8351 eV can be attributed to the pure dipoleallowed 1s→4p transition and the shoulder peak near which is attributed to the electronic dipole-allowed 1s→4p transition accompanied by ligand-to-metal charge transfer. The shift in edge energy is usually a result of changes in the valence state of the absorbing atoms.[44,45] In Figure 4b, the Ni K-edge gradually shifts to higher energy, while the intensity of the "white line" absorption peak is reduced at a charging voltage of 4.36 V, induced by the oxidation from Ni²⁺ to Ni⁴⁺. When further charging to 4.8 from 4.36 V, it is noted that the "white line" absorption peak remains constant, whereas the Ni K-edge absorption shifts slightly to lower energy, similar to the trend observed in ex situ XAS results in several previous works.[46-48] This phenomenon is related to the reduction of a small fraction of Ni⁴⁺, which is most likely caused by reduced coupling of Ni with oxygen, accompanied by oxidization of oxygen species in the vicinity.^[48,49] In contrast, the absorption edge of *n*-LMNO does not coincide with the pristine state when discharged to 2.0 V (Figure S11, Supporting Information), whereas they overlap exactly in d-LMNO (Figure 4b). It is illustrated that Ni possibly migrates from the stiff NiO6 octahedron sites to the Li-ion layer where it gets stuck during the charging-discharging process for n-LMNO, causing irreversible changes in the local structure. In sharp contrast, the variation in the absorption edge of the d-LMNO is highly flexible, manifesting that the Ni ions prefer to stabilize in the NiO₆ octahedral structure, thereby relieving the voltage fading to some extent.

The reversibility of structural change is also demonstrated by the EPR spectra at different lithiated states (Figure 4c). During the synthesis process of cathode materials, the partial Ni²⁺ ions in the metal layer inevitably migrate to the Li layer, resulting in Li/Ni mixing to some content. Consequently, three magnetic interactions including a linear Ni²⁺–O²⁻–Ni²⁺ (e_g-2p-e_g) antiferromagnetic (AF) super-exchange interaction mediated by oxygen

16146840, 2023, 5, Downloaded from https://adv

onlinelibrary.wiley.com/doi/10.1002/aenm.202203045 by University Town Of Shenzhen, Wiley Online Library on [20/11/2025]. See the Terms

and-conditions) on Wiley Online Library for rules of use; OA articles are governed by the applicable Creative Commons License

www.advancedsciencenews.com www.advenergymat.de

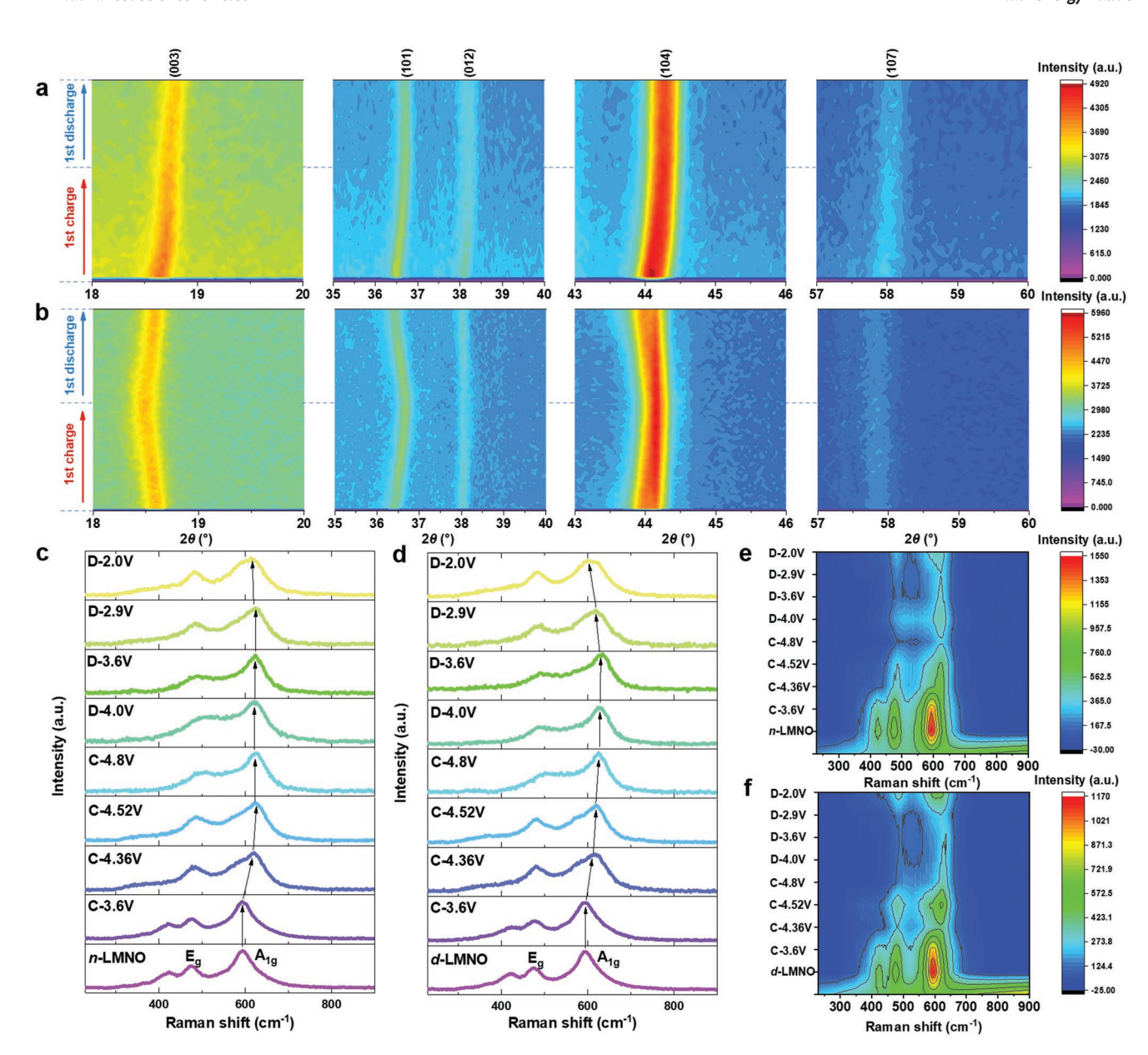


Figure 3. Characterization of structural reversibility in the first cycle of *d*-LMNO and *n*-LMNO. a,b) In situ XRD patterns of a) *n*-LMNO and b) *d*-LMNO. c,d) Ex situ Raman spectra of c) *n*-LMNO and d) *d*-LMNO during the first charge–discharge process in carefully designed voltage, and the corresponding contour images for e) *n*-LMNO and f) *d*-LMNO.

atoms, a linear Ni^{2+} – O^{2-} – Mn^{4+} (eg- 2 - 2 - 2) ferromagnetic (FM) interaction, and a 90° Ni^{2+} – O^{2-} – 2 - $^$

Ni⁴⁺ is reduced to Ni²⁺ and magnetic clusters around Ni²⁺ ions in the Li layer are partially restored, including the linear Ni²⁺– O²–Ni²⁺ AF super-exchange interaction, linear Ni²⁺–O²–Mn⁴⁺ FM interaction, and Ni²⁺–O²–Mn⁴⁺ interlayer connection same as the original compound, thus restoring the EPR signal. However, it is mentioned that the EPR signal after discharging to 2.0 V is obviously lower than the pristine state, as explained by Mn species. In fact, e⁻ is first absorbed by $(O_2)^{n-}$ with the discharge voltage above 3.0 V and then Mn⁴⁺ is further reduced to Mn³⁺ (non-EPR activity) by Mn-O spin coupling, resulting in a reduced EPR signal, as confirmed by in situ and ex situ EPR studies. [53,54] As a result, the nearly invariable EPR signals of *n*-LMNO after discharging to 2.0 V compared to charging to 4.8 V might be attributed to opposing actions of Ni and Mn

www.advenergymat.de

16146840, 2023, 5, Downloaded from https

onlinelibrary.wiley.com/doi/10.1002/aenm.202203045 by University Town Of Shenzhen, Wiley Online Library on [20/11/2025]. See the Terms and Conditions (https://onlinelibrary.wiley

on Wiley Online Library for rules of use; OA articles are governed by the applicable Creative Commons

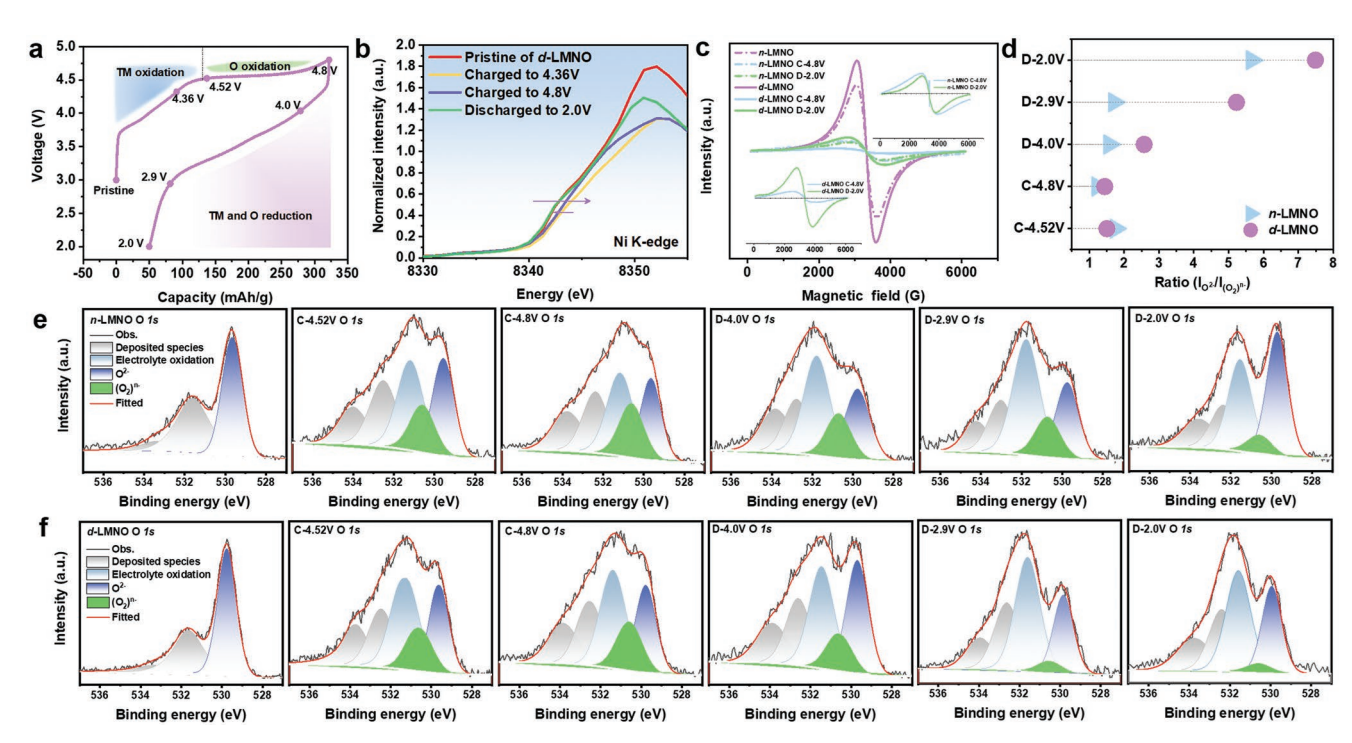


Figure 4. Local atomic structure variation in the electrochemical reaction process. a) The specific voltage in the first cycle and the TM and O redox reaction range during the charge and discharge process, the later ex situ characterization is obtained at the marked voltages. b) Ex situ Ni K-edge XAS spectra of d-LMNO upon first charging and discharging. c) Ex situ EPR spectra for d-LMNO and n-LMNO. d) The ratio of lattice oxygen (O²–) and oxygen species (O₂)^{n–} in the oxidized state calculated from XPS results. e,f) O 1s XPS spectra of e) n-LMNO and f) d-LMNO in the different charge/discharge states.

as mentioned above. In addition, it is further speculated that more $\mathrm{Mn^{4+}}$ in $n\text{-}\mathrm{LMNO}$ is likely reduced to $\mathrm{Mn^{3+}}$ considering its weaker EPR signal at 2.0 V than $d\text{-}\mathrm{LMNO}$, which is also supported by the observation of a more obvious $\mathrm{Mn^{3+}/Mn^{4+}}$ redox peak in the subsequent dQ/dV curves for $n\text{-}\mathrm{LMNO}$ (Figure 2e,f, and Figure S7, Supporting Information). Therefore, it is suggested that the reduction of $\mathrm{Mn^{4+}}$ to $\mathrm{Mn^{3+}}$ is responsible for the $\mathrm{O_2}$ release and TM migration, thus inducing a relatively serious voltage fading.

Besides XAS and EPR characterizations, ex situ XPS measurements were also performed to probe the states of oxygen species in d-LMNO and n-LMNO during the first charge and discharge process (Figure 4e,f). The main peaks observed near ≈529.5, ≈530.5, and ≈531.5 to 534 eV in the O 1s spectra are attributed to O^{2-} , $(O_2)^{n-}$ (n < 2), and various organic oxygen compounds generated by the decomposition of carbonate solvent, respectively. During the charging process, a similar trend is observed in both *n*-LMNO and *d*-LMNO that $(O_2)^{n-}$ species gradually increased with the rise of voltage. During the discharge process, the O²⁻ species appear prominently until 2.9 V for n-LMNO, while it restores immediately at 4.0 V for the d-LMNO (Figure 4d), again proving the sluggish anionic oxygen reduction in *n*-LMNO compared with *d*-LMNO. The O 1s XPS spectra further declare the superior reversibility for Li-defect structure, constituting a prerequisite for the long-term cycle for d-LMNO. Besides, it is observed that, although the locations of the peak in the Mn 2p XPS spectra scarcely change, the fitted curves after discharging to 2.0 V in the first cycle further demonstrate that more Mn³⁺ is formed for *n*-LMNO in comparison

with *d*-LMNO (Figure S12, Supporting Information). This further explains the more capacity contribution from $\mathrm{Mn^{3+}/Mn^{4+}}$ redox reactions in the dQ/dV curves for *n*-LMNO. Further, it is observed from the Ni 2p XPS spectrum that the peak change is not visible when charged to 4.8 V, while the peak of Ni 2p_{3/2} gradually emerges after discharging to 2.0 V for both *n*-LMNO and *d*-LMNO. Differently, the Ni 2p_{3/2} peak appears when the *d*-LMNO is discharged to 4.0 V, whereas it appears obtusely when discharged to 2.0 V (Figure S13, Supporting Information), demonstrative of superior reversibility of *d*-LMNO.

2.5. Structural Mechanism Interpretation

As clearly shown in **Figure 5**a, it is obtained from the DFT simulation that the crystal structure of *d*-LMNO shows lower energy when the closest coordination TM layer has more Ni surrounding the Li-defect site. And the energy barrier gives out a maximum value of -0.04 eV in the case that the four Ni coordination within the TM interlayer closest to the lithium-ion with Li defects compared with one Ni coordination (Figure 5a). In addition, it presents a lower energy barrier when lithium ions migrate to the lithium site where the closest coordination TM in the metal layer has more Ni coordination. Clearly, the Li-diffusion energy is the lowest in path 3, where the coordination TM closest to the diffused lithium-ion is four Ni coordination (Figure 5b). Also, the effect of two possible Li⁺ diffusion paths of oxygen dumbbell hopping (ODH) and tetrahedral site hopping (TSH),^[55] that is, Li-ions diffusing from one octahedral

16146840, 2023, 5, Downloaded from https://adv

elibrary.wikey.com/doi/10.1002/acams.202203045 by University Town Of Shenzhen, Wiley Online Library on [2011/2025]. See the Terms and Conditions (https://onlinelibrary.wiley.com/terms-and-conditions) on Wiley Online Library for rules of use; OA articles are governed by the applicable Creative Commons. License

www.advancedsciencenews.com www.advenergymat.de

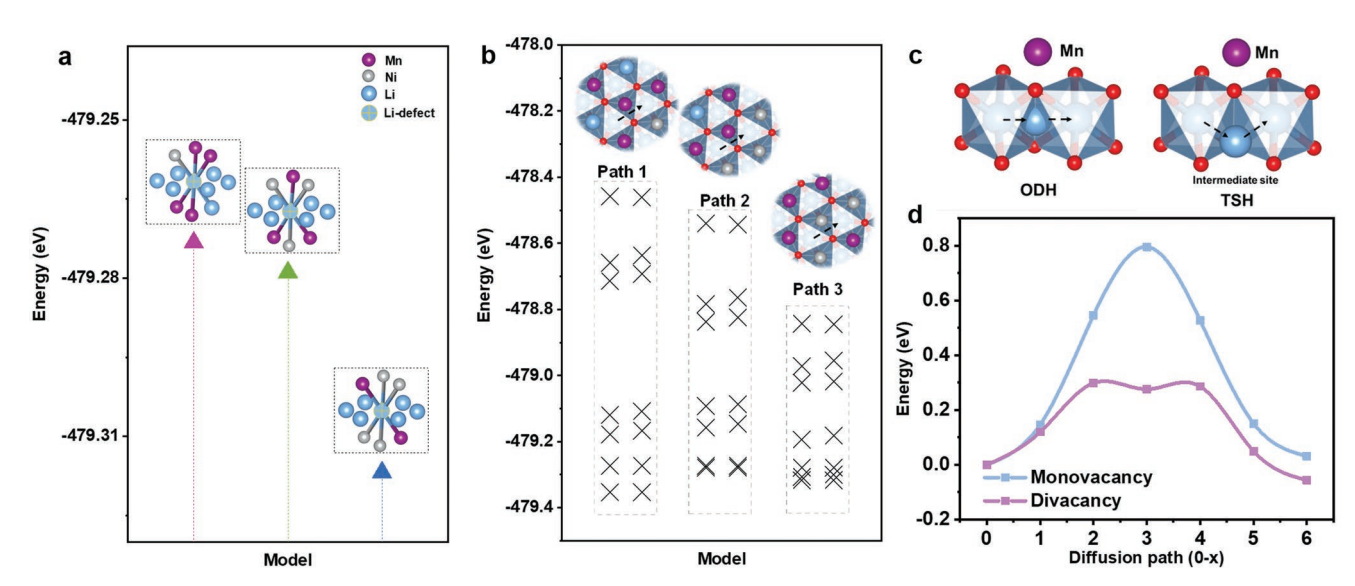


Figure 5. Structural models and the diffusion paths of d-LMNO and n-LMNO. a) The calculated energy of three possible structural models for Li-deficient Li_{1.2- σ}Mn_{0.6}Ni_{0.2}O₂ (d-LMNO). b) Li-diffusion paths by three kinds of TM orders within TM layers. c) The structural models of Li-diffusion along ODH and TSH paths. d) The calculated minimum energy barrier for Li_{1.2}Mn_{0.6}Ni_{0.2}O₂ and Li_{1.2- σ}Mn_{0.6}Ni_{0.2}O₂ from DFT based on monovacancy and divacancy, respectively.

site to the next by hopping directly through the oxygen dumbbell for ODH or via an intermediate tetrahedral site for TSH are simulated (Figure 5c). Further, the influence of the number of Li vacancies in the initial structure on Li migration has also been declared in Figure 5d. With regard to the Li migration in the case of one Li removal, when the Li octahedron surrounding the removed Li vacancy is occupied by Li-ion, the process of surrounding Li to migrate to the Li vacancy is dominated by ODH, and the corresponding migration energy barrier is high, indicating the slower migration rate in this case, which is known as single monovacancy migration. In the presence of additional vacancies around a removed Li vacancy, migration of the Li close to the vacancy is dominated by TSH, which has a low migration energy barrier. In consequence, it shows a lower energy barrier for Li migration when the initial structure contains some Li vacancies, which is consistent with higher Li-ion diffusion coefficients for d-LMNO (Figure 2c,d). Additionally, less interlayer Li/Ni disorder can be realized in the lithium-defect structure of *d*-LMNO (Figure S14, Supporting Information). Furthermore, it is clearly demonstrated that less interlayer Li/Ni disorder is beneficial to the preferred structural reversibility by the ex situ EPR and XAS results. Hence, it is proposed that d-LMNO with appropriate Li-defects is advantageous for reducing Ni migration from TM layers to Li-layers and limiting the interlayer Li/Ni disorder to mitigate voltage fading, oxygen release, and structure evolution during the initial charge process and such excellent structure stability is more conducive to the later cycle process.

2.6. Universality Demonstration of this CMISC Strategy for Improvement of Cobalt-Containing Li-rich Cathode

To demonstrate the universality of this strategy in creating lithium defects and improving electrochemical performance,

the cobalt-containing lithium-rich cathode materials of both $\text{Li}_{1.2-\sigma}\text{Mn}_{0.6}\text{Ni}_{0.1}\text{Co}_{0.1}\text{O}_2$ (d-LMNCO) and $\text{Li}_{1.2}\text{Mn}_{0.6}\text{Ni}_{0.1}\text{Co}_{0.1}\text{O}_2$ (n-LMNCO) are synthesized using the similar CMISC strategy and conventional method, respectively. As expected, d-LMNCO displays an improved first discharge capacity of 273 mAh g⁻¹ and an initial Coulombic efficiency of 77.0% at 0.1 C, in comparison with n-LMNCO (225.9 mAh g⁻¹ and 66.7%) (**Figure 6**a). Also, d-LMNCO retains a high capacity of 150 mAh g⁻¹ under a high current density of 5 C, indicative of favorable rate capability (Figure 6b). Moreover, the d-LMNCO offers a higher capacity and improved cyclability (180 mAh g⁻¹, 80.2%, Figure 6c) after 100 cycles than that of n-LMNCO (158.6 mAh g^{-1} , Figure S15, Supporting Information) at 1 C. Moreover, the ex situ XRD patterns (Figure 6d,e Figure S16, Supporting Information) and Raman measurements (Figure S17, Supporting Information) of d-LMNCO and n-LMNCO further verify the enhanced structural reversibility of d-LMNCO with lithium defects, similar to cobalt-free d-LMNO cathodes. In short, it is demonstrated that this CMISC strategy could also improve the comprehensive performance of the cobalt-containing Li-rich materials, possessing great universality.

3. Conclusion

In summary, a general long-neglected Li-defect construction strategy is demonstrated to alleviate the issues of low initial Coulombic efficiency and poor cycling stability in Li-rich cathode materials. The modified d-LMNO with appropriate Li defects achieves significantly improved performance including a high specific capacity of 272 mAh g $^{-1}$, excellent initial Coulombic efficiency of 84.5%, and 82.0% capacity retention after 200 cycles, remarkably exceeding the n-LMNO. In addition, diverse characterizations and theoretical simulation further confirm the appropriate lithium depletion regulated 3d-transition

16146840, 2023, 5, Downloaded from https://advanced.

onlinelibrary.wiley.com/doi/10.1002/aenm.202203045 by University Town Of Shenzhen, Wiley Online Library on [20/11/2025]. See the Terms

and-conditions) on Wiley Online Library for rules of use; OA articles are governed by the applicable Creative Commons

www.advancedsciencenews.com

www.advenergymat.de

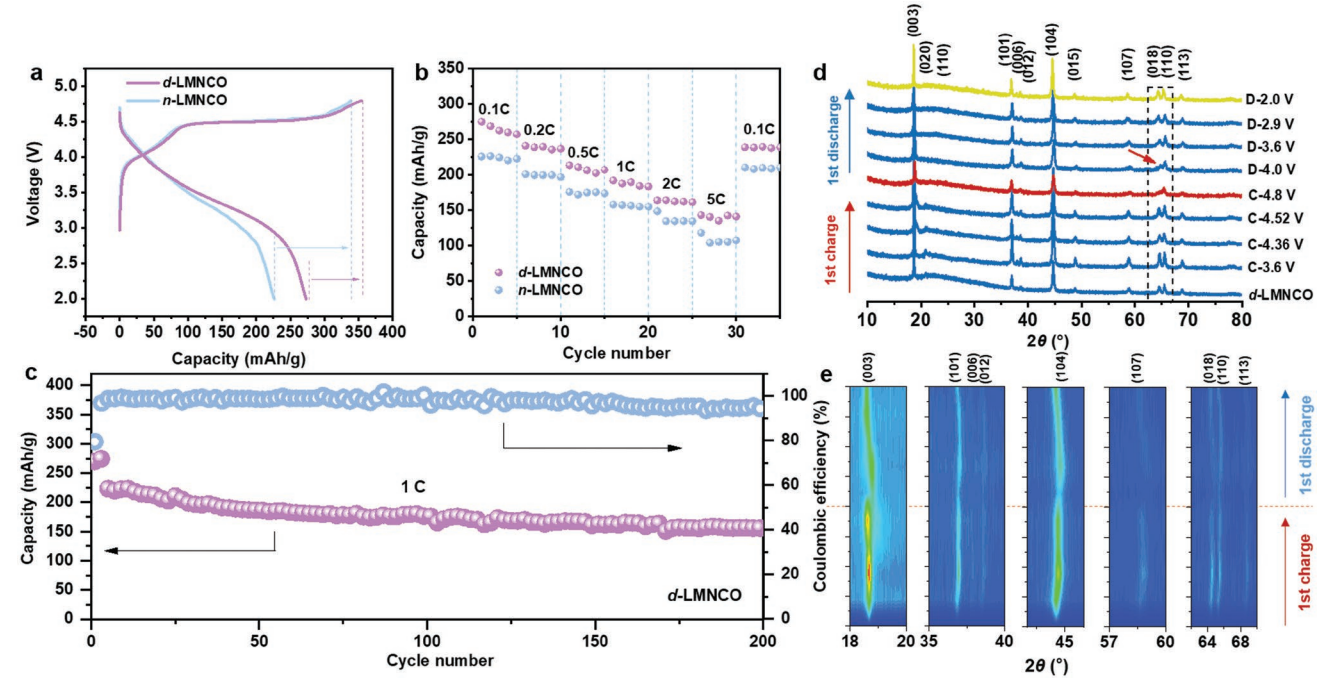


Figure 6. Electrochemical performance and structural characterizations of cobalt-containing Li-rich cathode materials. a) The charge-discharge profiles in the first cycle of $Li_{1.2-\sigma}Mn_{0.6}Ni_{0.1}Co_{0.1}O_2$ (d-LMNCO) and $Li_{1.2}Mn_{0.6}Ni_{0.1}Co_{0.1}O_2$ (d-LMNCO) and d-LMNCO bested at 0.1 C. b) Rate performance of d-LMNCO and d-LMNCO. c) Cyclic stability of d-LMNCO obtained at 1 C. d) Ex situ XRD patterns of d-LMNCO during the first charge-discharge process and e) the color-coded images (below).

metal interlayered disorder, resulting in the excellent structural reversibility and diffusion kinetics of *d*-LMNO. Importantly, this CMISC method is highly universal and applicable for generating Li defects in both cobalt-free and cobalt-containing Li-rich cathodes. We believe these results will inspire the researchers to reconsider this route for enhancing initial Coulombic efficiency and cycle stability and promote practical applications of Li-rich cathode materials in the near future.

Supporting Information

Supporting Information is available from the Wiley Online Library or from the author.

Acknowledgements

This work was financially supported by the National Key R&D Program of China (Grant 2022YFA1504100), the National Natural Science Foundation of China (Grant Nos. 22279137, 22125903, 51872283, 22075279), the "Transformational Technologies for Clean Energy and Demonstration" Strategic Priority Research Program of the Chinese Academy of Sciences (Grant No. XDA21000000), Dalian Innovation Support Plan for High Level Talents (2019RT09), Dalian National Laboratory For Clean Energy (DNL), CAS, DNL Cooperation Fund, CAS (DNL202016, DNL202019), and DICP (DICP I2020032), the Joint Fund of the Yulin University and the Dalian National Laboratory for Clean Energy (YLU-DNL Fund 2021002, 2021009).

Conflict of Interest

The authors declare no conflict of interest.

Data Availability Statement

Research data are not shared.

Keywords

calcination medium-induced surface-corrosion, initial efficiency, Li-depletion, Li-rich materials, structural reversibility

Received: September 6, 2022 Revised: November 22, 2022 Published online: December 20, 2022

- [1] J. Lee, D. A. Kitchaev, D. H. Kwon, C. W. Lee, J. K. Papp, Y. S. Liu, Z. Lun, R. J. Clement, T. Shi, B. D. McCloskey, J. Guo, M. Balasubramanian, G. Ceder, *Nature* 2018, 556, 185.
- [2] T. Liu, L. Yu, J. Liu, J. Lu, X. Bi, A. Dai, M. Li, M. Li, Z. Hu, L. Ma, D. Luo, J. Zheng, T. Wu, Y. Ren, J. Wen, F. Pan, K. Amine, Nat. Energy 2021, 6, 277.
- [3] M. F. Toney, Nat. Energy 2019, 4, 1014.
- [4] G. Assat, S. L. Glazier, C. Delacourt, J.-M. Tarascon, Nat. Energy 2019, 4, 647.
- [5] M. Sathiya, G. Rousse, K. Ramesha, C. P. Laisa, H. Vezin, M. T. Sougrati, M. L. Doublet, D. Foix, D. Gonbeau, W. Walker, A. S. Prakash, M. Ben Hassine, L. Dupont, J. M. Tarascon, *Nat. Mater.* 2013, 12, 827.
- [6] M. Sathiya, A. M. Abakumov, D. Foix, G. Rousse, K. Ramesha, M. Saubanere, M. L. Doublet, H. Vezin, C. P. Laisa, A. S. Prakash, D. Gonbeau, G. VanTendeloo, J. M. Tarascon, *Nat. Mater.* 2015, 14, 230.
- [7] J. Xu, M. Sun, R. Qiao, S. E. Renfrew, L. Ma, T. Wu, S. Hwang, D. Nordlund, D. Su, K. Amine, J. Lu, B. D. McCloskey, W. Yang, W. Tong, Nat. Commun. 2018, 9, 947.

ADVANCED ENERGY

16146484, 2023, 5, Downloaded from https://advanced.onlinelibitrary.wiely.com/doi/10.1002/aema.022.03045 by University Town Of Shenzhen, Wiley Online Library on [20/11/2025]. See the Terms and Conditions (https://onlinelibitrary.viely.com/terms-and-conditions) on Wiley Online Library for rules of use; OA articles are governed by the applicable Creative Commons.

www.advancedsciencenews.com www.advenergymat.de

- [8] F. Ning, B. Li, J. Song, Y. Zuo, H. Shang, Z. Zhao, Z. Yu, W. Chu, K. Zhang, G. Feng, X. Wang, D. Xia, Nat. Commun. 2020, 11, 4973.
- [9] R. Sharpe, R. A. House, M. J. Clarke, D. Forstermann, J. J. Marie, G. Cibin, K. J. Zhou, H. Y. Playford, P. G. Bruce, M. S. Islam, J. Am. Chem. Soc. 2020, 142, 21799.
- [10] E. Hu, X. Yu, R. Lin, X. Bi, J. Lu, S. Bak, K.-W. Nam, H. L. Xin, C. Jaye, D. A. Fischer, K. Amine, X.-Q. Yang, *Nat. Energy* **2018**, *3*, 690
- [11] P. E. Pearce, A. J. Perez, G. Rousse, M. Saubanere, D. Batuk, D. Foix, E. McCalla, A. M. Abakumov, G. Van Tendeloo, M. L. Doublet, J. M. Tarascon, *Nat. Mater.* 2017, *16*, 580.
- [12] J. Hong, W. E. Gent, P. Xiao, K. Lim, D. H. Seo, J. Wu, P. M. Csernica, C. J. Takacs, D. Nordlund, C. J. Sun, K. H. Stone, D. Passarello, W. Yang, D. Prendergast, G. Ceder, M. F. Toney, W. C. Chueh, *Nat. Mater.* 2019, *18*, 256.
- [13] D. Mohanty, J. Li, D. P. Abraham, A. Huq, E. A. Payzant, D. L. Wood, C. Daniel, Chem. Mater. 2014, 26, 6272.
- [14] K. Kleiner, B. Strehle, A. R. Baker, S. J. Day, C. C. Tang, I. Buchberger, F.-F. Chesneau, H. A. Gasteiger, M. Piana, *Chem. Mater.* 2018, 30, 3656
- [15] W. E. Gent, K. Lim, Y. Liang, Q. Li, T. Barnes, S. J. Ahn, K. H. Stone, M. McIntire, J. Hong, J. H. Song, Y. Li, A. Mehta, S. Ermon, T. Tyliszczak, D. Kilcoyne, D. Vine, J. H. Park, S. K. Doo, M. F. Toney, W. Yang, D. Prendergast, W. C. Chueh, *Nat. Commun.* 2017. 8, 2091.
- [16] S. Myeong, W. Cho, W. Jin, J. Hwang, M. Yoon, Y. Yoo, G. Nam, H. Jang, J. G. Han, N. S. Choi, M. G. Kim, J. Cho, *Nat. Commun.* 2018, 9, 3285.
- [17] K. Nakayama, R. Ishikawa, S. Kobayashi, N. Shibata, Y. Ikuhara, Nat. Commun. 2020, 11, 4452.
- [18] N. Li, S. Hwang, M. Sun, Y. Fu, V. S. Battaglia, D. Su, W. Tong, Adv. Energy Mater. 2019, 9, 1902258.
- [19] B. Li, M. T. Sougrati, G. Rousse, A. V. Morozov, R. Dedryvere, A. Iadecola, A. Senyshyn, L. Zhang, A. M. Abakumov, M. L. Doublet, J. M. Tarascon, *Nat. Chem.* 2021, 13, 1070.
- [20] F. Dogan, B. R. Long, J. R. Croy, K. G. Gallagher, H. Iddir, J. T. Russell, M. Balasubramanian, B. Key, J. Am. Chem. Soc. 2015, 137, 2328.
- [21] R. A. House, G. J. Rees, M. A. Pérez-Osorio, J.-J. Marie, E. Boivin, A. W. Robertson, A. Nag, M. Garcia-Fernandez, K.-J. Zhou, P. G. Bruce, Nat. Energy 2020, 5, 777.
- [22] J. Zheng, P. Xu, M. Gu, J. Xiao, N. D. Browning, P. Yan, C. Wang, J.-G. Zhang, Chem. Mater. 2015, 27, 1381.
- [23] D. Eum, B. Kim, S. J. Kim, H. Park, J. Wu, S. P. Cho, G. Yoon, M. H. Lee, S. K. Jung, W. Yang, W. M. Seong, K. Ku, O. Tamwattana, S. K. Park, I. Hwang, K. Kang, Nat. Mater. 2020, 19, 419.
- [24] A. J. Perez, Q. Jacquet, D. Batuk, A. Iadecola, M. Saubanère, G. Rousse, D. Larcher, H. Vezin, M.-L. Doublet, J.-M. Tarascon, *Nat. Energy* 2017, 2, 954.
- [25] R. A. House, J. J. Marie, J. Park, G. J. Rees, S. Agrestini, A. Nag, M. Garcia-Fernandez, K. J. Zhou, P. G. Bruce, *Nat. Commun.* 2021, 12, 2975.
- [26] R. Lin, E. Hu, M. Liu, Y. Wang, H. Cheng, J. Wu, J. C. Zheng, Q. Wu, S. Bak, X. Tong, R. Zhang, W. Yang, K. A. Persson, X. Yu, X. Q. Yang, H. L. Xin, *Nat. Commun.* 2019, 10, 1650.
- [27] Y. Shin, W. H. Kan, M. Aykol, J. K. Papp, B. D. McCloskey, G. Chen, K. A. Persson, Nat. Commun. 2018, 9, 4597.
- [28] Q. Chen, Y. Pei, H. Chen, Y. Song, L. Zhen, C. Y. Xu, P. Xiao, G. Henkelman, Nat. Commun. 2020, 11, 3411.

- [29] J. Zhang, Q. Zhang, D. Wong, N. Zhang, G. Ren, L. Gu, C. Schulz, L. He, Y. Yu, X. Liu, Nat. Commun. 2021, 12, 3071.
- [30] J. Huang, P. Zhong, Y. Ha, D.-H. Kwon, M. J. Crafton, Y. Tian, M. Balasubramanian, B. D. McCloskey, W. Yang, G. Ceder, *Nat. Energy* 2021, 6, 706.
- [31] T. Liu, J. Liu, L. Li, L. Yu, J. Diao, T. Zhou, S. Li, A. Dai, W. Zhao, S. Xu, Y. Ren, L. Wang, T. Wu, R. Qi, Y. Xiao, J. Zheng, W. Cha, R. Harder, I. Robinson, J. Wen, J. Lu, F. Pan, K. Amine, *Nature* 2022, 606, 305.
- [32] D. Eum, B. Kim, J.-H. Song, H. Park, H.-Y. Jang, S. J. Kim, S.-P. Cho, M. H. Lee, J. H. Heo, J. Park, Y. Ko, S. K. Park, J. Kim, K. Oh, D.-H. Kim, S. J. Kang, K. Kang, Nat. Mater. 2022, 21, 664.
- [33] D. H. Seo, J. Lee, A. Urban, R. Malik, S. Kang, G. Ceder, *Nat. Chem.* 2016. 8, 692.
- [34] Y. Xie, M. Saubanère, M. L. Doublet, *Energy Environ. Sci.* **2017**, *10*, 266.
- [35] J. H. Song, G. Yoon, B. Kim, D. Eum, H. Park, D. H. Kim, K. Kang, Adv. Energy Mater. 2020, 10, 2001207.
- [36] Y. Zhang, Y. Gao, F. Yu, Q. Wang, Chem. Eng. J. 2019, 371, 424.
- [37] M. Xiang, Y. Zhang, Y. Zhang, C. Wang, Y. Yu, Fusion Eng. Des. 2016, 102, 1.
- [38] D. Liu, X. Fan, Z. Li, T. Liu, M. Sun, C. Qian, M. Ling, Y. Liu, C. Liang, Nano Energy 2019, 58, 786.
- [39] G. Sun, F. D. Yu, C. Zhao, R. Yu, S. Farnum, G. Shao, X. Sun, Z. B. Wang, Adv. Funct. Mater. 2020, 31, 2002643.
- [40] G. Assat, D. Foix, C. Delacourt, A. Iadecola, R. Dedryvere, J. M. Tarascon, Nat. Commun. 2017, 8, 2219.
- [41] M. Chen, X. Jin, Z. Chen, Y. Zhong, Y. Liao, Y. Qiu, G. Cao, W. Li, J. Mater. Chem. A 2019, 7, 13120.
- [42] J. An, L. Shi, G. Chen, M. Li, H. Liu, S. Yuan, S. Chen, D. Zhang, J. Mater. Chem. A 2017, 5, 19738.
- [43] R. A. House, J.-J. Marie, M. A. Pérez-Osorio, G. J. Rees, E. Boivin, P. G. Bruce, Nat. Energy 2021, 6, 781.
- [44] K.-W. Nam, S.-M. Bak, E. Hu, X. Yu, Y. Zhou, X. Wang, L. Wu,
- Y. Zhu, K.-Y. Chung, X.-Q. Yang, Adv. Funct. Mater. 2013, 23, 1047. [45] W. Yoon, M. Balasubramanian, K. Chung, X. Yang, J. Mcbreen,
- C. Grey, D. Fischer, J. Am. Chem. Soc. 2005, 127, 17479.
 [46] S. Muhammad, H. Kim, Y. Kim, D. Kim, J. H. Song, J. Yoon, J.-H. Park, S.-J. Ahn, S.-H. Kang, M. M. Thackeray, W.-S. Yoon, Nano

Energy 2016, 21, 172.

- [47] N. Yabuuchi, K. Yoshii, S. T. Myung, I. Nakai, S. Komaba, J. Am. Chem. Soc. 2011, 133, 4404.
- [48] D. Dixon, S. Mangold, M. Knapp, H. Ehrenberg, A. Bhaskar, Adv. Energy Mater. 2021, 11, 2100479.
- [49] E. J. Kim, L. A. Ma, L. C. Duda, D. M. Pickup, A. V. Chadwick, R. Younesi, J. T. S. Irvine, A. R. Armstrong, ACS Appl. Energy Mater. 2019, 3, 184
- [50] J. Zheng, G. Teng, C. Xin, Z. Zhuo, J. Liu, Q. Li, Z. Hu, M. Xu, S. Yan, W. Yang, F. Pan, J. Phys. Chem. Lett. 2017, 8, 5537.
- [51] N. A. Chernova, M. Ma, J. Xiao, M. S. Whittingham, J. Breger, C. P. Grey, Chem. Mater. 2007, 19, 4682.
- [52] H. Nguyen, R. J. Clément, ACS Energy Lett. 2020, 5, 3848.
- [53] M. Tang, A. Dalzini, X. Li, X. Feng, P. H. Chien, L. Song, Y. Y. Hu, J. Phys. Chem. Lett. 2017, 8, 4009.
- [54] A. Niemoller, P. Jakes, S. Eurich, A. Paulus, H. Kungl, R. A. Eichel, J. Granwehr, J. Chem. Phys. 2018, 148, 014705.
- [55] Y. Wei, J. Zheng, S. Cui, X. Song, Y. Su, W. Deng, Z. Wu, X. Wang, W. Wang, M. Rao, Y. Lin, C. Wang, K. Amine, F. Pan, J. Am. Chem. Soc. 2015, 137, 8364.